Research Article

Precise State-of-Charge Mapping via Deep Learning on Ultrasonic Transmission Signals for Lithium-Ion Batteries

Zhenyu Huang,[§] Yu Zhou,[§] Zhe Deng, Kai Huang, Mingkang Xu, Yue Shen,* and Yunhui Huang*

Cite This: *ACS Appl. Mater. Interfaces* 2023, 15, 8217–8223

Read Online

ACCESS | 📊 Metrics & More | 📖 Article Recommendations | 🔵 Supporting Information

ABSTRACT: The uneven distribution of state of charge (SoC) in the lithium-ion battery is a key factor to cause fast decay of local electrochemical performance. Here, we report an acoustic method to realize SoC mapping in a pouch cell. A focused ultrasound beam is used to scan the cell, and the transmitted ultrasonic wave is analyzed with a deep learning algorithm based on the feedforward neural network. The deep learning algorithm effectively suppresses the disturbance of structural variation in different cells. As a result, the root mean squared error (RMSE) of the estimated local SoC is reduced to 3.02% when applying to different positions on different pouch cells, which is 11.07% of the RMSE by direct fitting SoC with acoustic time of flight. Combining with the progressive scanning technique, our method can realize non-destructive *in situ* SoC mapping with 1 mm in-plane resolution on pouch cells.
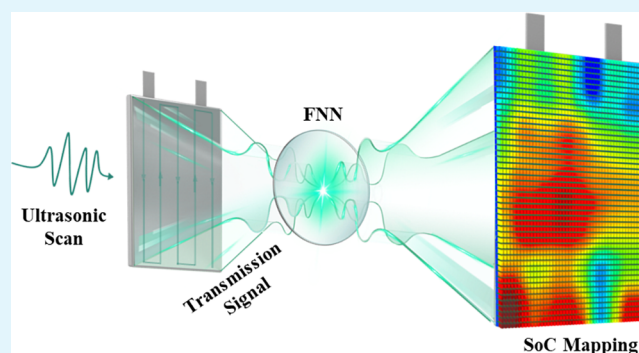
Lithium-ion battery (LIB) is a widely used electrochemical energy storage device. Ideally, we hope that the entire cell undergoes uniform discharge/charge during operation so that the state of charge (SoC) is evenly distributed in the cell. However, in many reports, researchers have found that the state of charge in the lithium-ion battery is not the same at different parts of the cell. This phenomenon may be caused by many reasons, such as fluctuation of electrode/separating membrane porosity, insufficient electrolyte wetting, local gas bubbles, nonuniform SEI formation, temperature inhomogeneity, *etc.* Inhomogeneous SoC distribution is known to be harmful to cycle life because it means that some part of the cell always operates at a relatively high SoC region, which may cause accelerated electrode deterioration, electrolyte consumption, and active lithium loss. Therefore, it is crucial to visualize the inhomogeneous SoC distribution of the cell. However, this is quite a challenging task because LIB cells have complex structures closely packed will shells.

Various methods have been used to characterize the heterogeneity SoC distributions of electrodes at different scales,[1,2] including Raman spectroscopy,[3−8] neutron diffraction,[9−11] scanning transmission X-ray microscopy,[12,13] high-energy synchrotron X-ray,[14] synchrotron X-ray diffraction,[15] X-ray absorption near edge structure,[16,17] and colorimetric[18] and scanning ion conductance microscopy.[19] These methods have demonstrated that inhomogeneous SoC distribution is indeed a common issue in LIBs. The SoC variation can be as large as 20% in a single cell.[15] However, due to the low transmissivity of light, electron-beam, and even X-ray, these methods usually

need to disassemble the cells before examination, which are not applicable for online SoC mapping of commercial large cells.

On the other hand, Steingart and co-workers[20] have demonstrated that the time of flight (ToF) and intensity of transmitted ultrasound are sensitive to LIB SoC. After that, researchers have put much effort to develop acoustic methods for SoC estimation and have gotten many positive results.[21−26] Since an ultrasonic beam has excellent transmissivity in LIBs, it is natural to think that ultrasonic scanning should be a promising way to realize nondestructive *in situ* SoC mapping. In this work, we demonstrate that this technical route is feasible. However, because the transmission of ultrasound is influenced by many factors other than SoC, which may differ from cell to cell, it is impossible to obtain accurate SoC of different cells via direct fitting with simple ultrasonic characteristics, e.g., ToF, intensity, or frequency. To solve this problem, a deep learning algorithm based on the feedforward neural network (FNN) is developed to analyze the entire waveform instead of simple acoustic characteristics so that the SoC value can be extracted from complicated
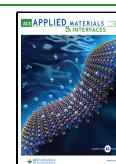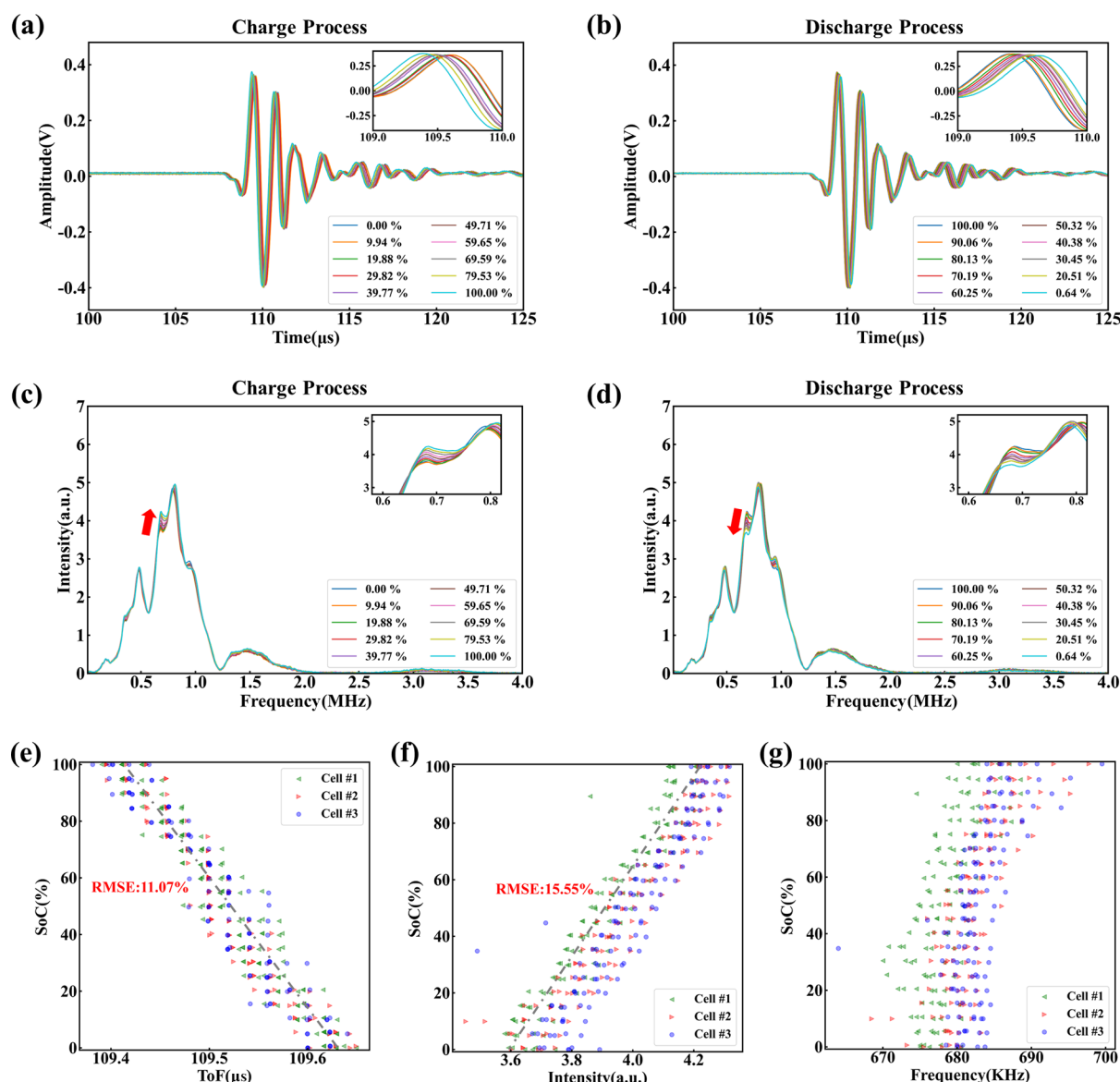
Figure 1. Acoustic response to SoC change. (a, b) Time domain transmitted ultrasonic waveform through Cell #1 at different SoCs during charge (a) and discharge (b); (c, d) frequency domain ultrasonic signal through Cell #1 at different SoCs during charge (c) and discharge (d); (e) correlation between SoC and ultrasound ToF through three different cells; (f, g) correlation between SoC and intensity (f) and summit frequency (g) of ~0.7 MHz shoulder peak in three different cells. The details of data collection are described in the Supporting Information: Data for Acoustic Response to SoC Changing section.

factors. As a result, the root mean squared error (RMSE) of estimated SoC was reduced to 3.02% when applying to different pouch cells. Combining with the focused ultrasonic beam progressive scanning technique, our method can realize non-destructive SoC mapping with 1 mm in-plane resolution on pouch cells.

At first, the relationship between the transmitted ultrasonic signal and SoC was studied during charge and discharge. Three $LiCoO_2$-graphite pouch cells with a rolled electrode structure were tested with a 1 MHz wide-band focused ultrasonic beam in the TOPS-LD50A ultrasonic battery scanning system. The detailed system components are shown in Table S1. The detailed cell structure is described in Table S2. All cells were immersed in silicone oil bath to minimize ultrasound attenuation out of the cells. The charge/discharge processes were divided into 20 segments. For each segment, the cell was depolarized for 20 min and then tested with ultrasound for 5

min (the details are described in the Supporting Information: Testing Procedure and Data Collection section). The detailed charge/discharge protocol is shown in Table S3. The voltage-capacity curves are shown in Figure S2.

At a certain position on a typical cell (Cell #1), the transmitted ultrasonic waveforms are shown in Figure 1. In the time domain figures (Figure 1a,b), it is clearly shown that the ToF of the ultrasonic wave shifts to a lower value during charge and shifts back during discharge. Meanwhile, the PPV of the wave did not change very much. These results are generally consistent with previous reports.[20−26] It was reported that the delithiation/lithiation behaviors of the Li_xCoO_2 cathodes and graphite anodes would induce variations in electrode thickness (d), density (ρ), Young's modulus (E), and Poisson's ratio (σ). These factors would further change the acoustic impedance of the full cell and influence the ToF and transmitted sound intensity.
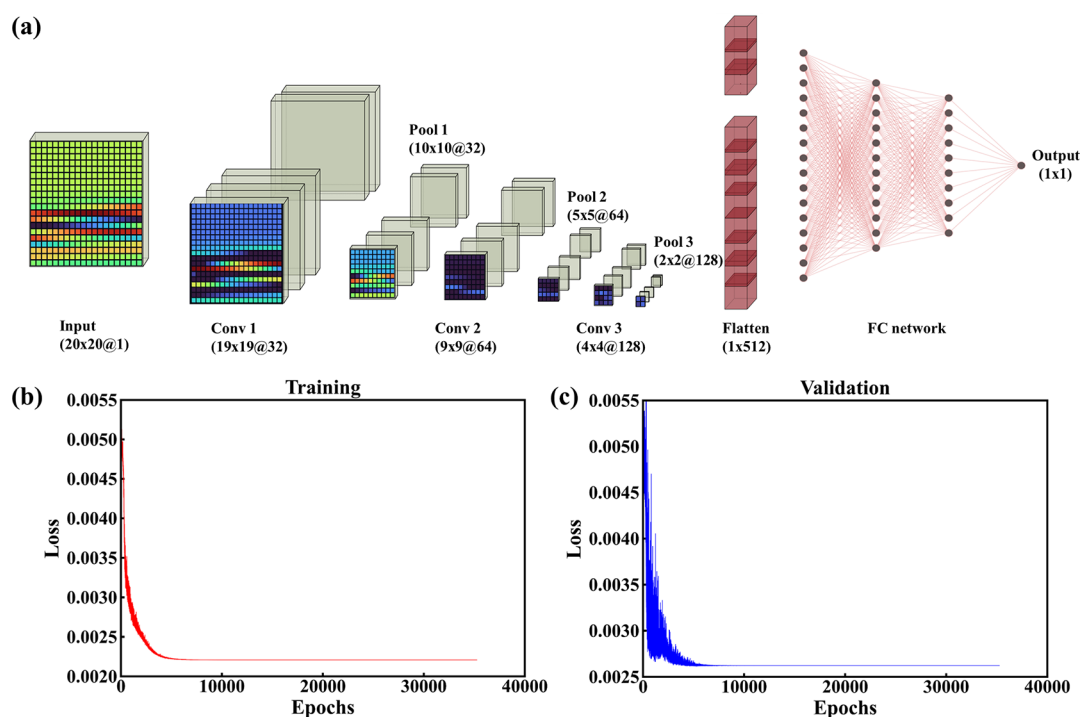
Figure 2. (a) Schematic illustration of the FNN structure; (b, c) loss convergence trend on the training dataset (b) and validation dataset (c).

The acoustic intensity and frequency evolution were more obvious on the frequency domain curves, which were obtained via Fourier transformation of the measured time domain curves (Figure 1c,d). The curves presented a wide frequency band. The summit of the frequency band was at around 0.8 MHz, which did not change significantly during charge/discharge. Meanwhile, there was a shoulder peak at around 0.7 MHz, which varied significantly during charge/discharge. In the charge process, the accurate position of the shoulder peak shifted to higher frequency, and the peak intensity increased significantly. In the following discharge process, these changes were completely reversible.

According to the above results, the ToFs measured from the time domain curve, the frequency, and intensity of the shoulder peak on the frequency domain curve are demonstrated as three independent characteristics potentially applicable to predict the SoC of the battery. To evaluate which characteristic has the most robust correlation with SoC, the ultrasonic measurement was extended to different positions on different pouch cells to test the consistency. The correlations between different acoustic characteristics and SoC are shown in Figure 1e−g. The spots of different colors represent measurements of different cells.

Ideally, we expect these spots to be distributed on a narrow line so that we can read the accurate SoC on the Y axis according to the acoustic characteristic value on the X axis. However, the results were not satisfying. All of these acoustic characteristics exhibited weak correlation with SoC, especially when the data were collected from measurements of different cells.

The correlation between SoC and ToF is shown in Figure 1e. The variation of SoC corresponding to a certain ToF was very large, especially on different cells. If the SoC is estimated via linear fitting of SoC-ToF data measured from Cell #1, then the RMSE would be as large as 11.07% when applying to three different cells. Such a big error makes this method incapable of

monitoring the status of an unknown cell or studying the SoC distribution.

The correlation between SoC and intensity/frequency of the shoulder peak around 0.7 MHz was even worse. In Figure 1f, the RMSE of the estimated SoC was as high as 15.55% via linear fitting of SoC-intensity data measured from Cell #1. In Figure 1g, the SoC value even varied from 0 to 100% in the frequency region of 680−685 KHz. Obviously, it is impossible to obtain accurate SoC.

According to the above results, we conclude that although some characteristics of the transmitted ultrasonic wave vary with SoC, the correlations between these characteristics and SoC are not robust enough to obtain accurate SoC. This problem is because the transmission of ultrasound is influenced by many factors other than SoC, e.g., the compact density of the electrode or separating membrane, the local electrolyte wetting status, the local formation quality, the contact between the aluminum-plastic film and the jelly roll, and even the mounting posture of the cell in the ultrasonic scanner. It is very difficult to keep all these factors completely unchanged during cell production. The measured ultrasonic wave is a general reflection of many structural characteristics of the cell, including but not limited to SoC. To predict the SoC value of an unknown cell, it is necessary to use some "data mining" technique to dig out the SoC value from the complicated ultrasonic waveform.

To solve the above problem, deep learning is induced to analyze the entire waveform instead of fitting with simple acoustic characteristics. Deep learning a class of machine learning algorithms uses multiple layers to progressively extract higher-level features from a complicated raw input. It has achieved huge success in computer vision, speech recognition, natural language processing, machine translation, etc. Previously, Brett *et al.*[21] have reported that deep learning is capable of improving the SoC estimation accuracy of a specific LIB cell. Here, we have optimized the algorithms with a

supervised learning strategy and successfully extracted a high accuracy local SoC value from ultrasonic measurements at different positions on different cells.

Our deep learning algorithms are based on a FNN that contains a convolutional neural network (CNN) with three convolutional layers and three pooling layers and a fully connected neural network (FCNN), as shown in Figure 2a. The CNN can self-extract significant features and has a very high efficiency in the weight optimization process, and the FCNN has a very strong non-linear fitting ability. These merits are important for SoC estimation. Inspired by previous works,[21,24,27−30] we have made many efforts to optimize the neural network structure as well as the hyperparameters: the raw acoustic data was pretreated with the variance filtering method to eliminate irrelevant features so that the computational complexity was reduced and the model training time was shortened (the details are described in the Supporting Information: Variance Filtering section); the weight initialization method was optimized to make the model update weights in the right direction from the training initiation (the details are described in the Supporting Information: Weight Initialization section); a dynamic adjustment method of the learning rate was used to avoid model falling into the local optimum and reduce SoC estimation error (the details are described in the Supporting Information: Dynamically Adjusting the Learning Rate section); proper regularization items were added to suppress overfitting, which improves the estimation accuracy on unknown cells (the details are described in the Supporting Information: Regularization Items section).

The training dataset was collected from the measurements of 150 randomly chosen positions on Cell #5 under 42 general SoCs (the details of data collection are described in the Supporting Information: Data for FNN Model Training section), and the "general SoCs" refer to the SoCs measured with the ampere integral of the full cells. Therefore, 6300 groups of single-point acoustic data were obtained, and the label SoC of each group is equal to the general SoC of the cell. Each single-point acoustic data is a 10,000-length vector, which was shown as black dots in Figure S5. By taking the variance filtering method, the number of the acoustic data was reduced from 10,000 to 400 (A_I') in this manner; then, we converted the acoustic data from 1D vectors to 2D matrices (B') for better 2D convolution operations, and the data left behind was indicated by a red dotted line in Figure S5.

$$A_I' = [\beta_1, \beta_2, \ldots \beta_1, \ldots, \beta_{400}]$$

where β_i is one of the data in the 10,000-length vector acoustic data, which was maintained after variance filtering.

$$B' = \begin{bmatrix} \beta_{1,1} & \cdots & \beta_{1,20} \\ \vdots & \ddots & \vdots \\ \beta_{20,1} & \cdots & \beta_{20,20} \end{bmatrix}$$

Then, the dataset and SoC label were shown like below:

$$X = [B_1', B_2', \ldots, B_{6300}']$$

$$Y = [S_1, S_2, \ldots, S_{6300}]$$

where B_i' is a 2D matrix format acoustic data from one spatial position on the cell and S_i is equal to the general SoC at which B_i' was collected. The data was separated for training and

testing, and the proportion of training is 0.75, which implies that the training dataset length is 4725 and the testing dataset length is 1575. Then, we shuffled the order of the input dataset and SoC label to improve the generalization ability and obtain proper weight initialization to make the network training stage be more stable and efficient. As a result, the FNN model converged after 35,251 epochs of iterations, and the convergence trends of the loss function on both the training and validation dataset were as expected (Figure 2b,c).

The FNN estimated local SoC was compared with the ICP-OES measured local lithium content in the anodes. Three cells were charged to 30% (Cell #4), 50% (Cell #5), and 70% (Cell #6). Then, these cells were disassembled and the anodes were punched with a 6 mm puncher at six different positions, as indicated in Figure 3. For each position, three layers of anodes
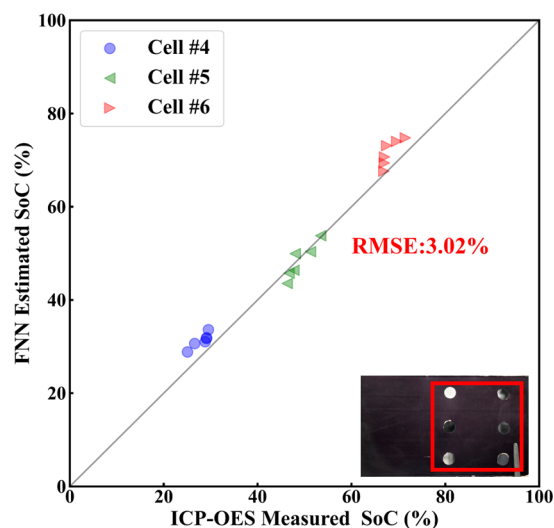

Figure 3. Comparison of the FNN estimated local SoC and inductively coupled plasma-optical emission spectrometry (ICP-OES) measured local SoC value at different positions on Cell #4, Cell #5, and Cell #6, of which the general SoCs were 30, 50, and 70%, respectively. The details of data collection are described in the Supporting Information: Data for FNN Estimated Local SoC section.

were punched. The lithium contents of the obtained anode pellets were measured with ICP-OES. The details of the sample preparation are described in the Supporting Information (Figure S6). According to the measured lithium contents, the local SoCs at these positions were calculated via eq S5.

As a result, the FNN estimated SoC and ICP-OES measured SoC agreed quite well. All of the data points were distributed close to the gray diagonal line in Figure 3. During the FNN model iterative adjustment process, these methods (data variance filtering, weight initialization, dynamically adjusting the learning rate, and regularization items) we mentioned above have been proven to be effective in improving the accuracy of SoC estimation; the details are indicated in Figure S7. The Euclid distance similarities of the FNN estimated SoCs and the ICP-OES method SoCs at the six positions on three cells (Cell #4, Cell #5, and Cell #6) were 0.924, 0.963, and 0.917, respectively, indicating that the correlation between the FNN estimated SoCs and ICP-OES measured SoCs was very strong, even in different cells. The root mean squared error (RMSE) of SoC estimation was reduced to 3.02%, indicating that the optimized FNN algorithms have excellent
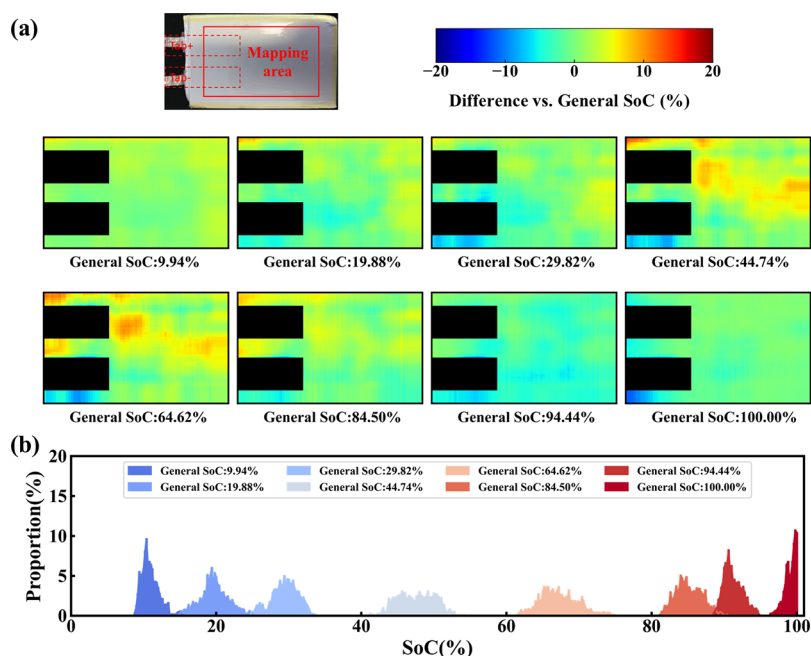
Figure 4. (a) SoC mapping of Cell #4 during charge. (b) Histograms of SoC distribution at different general SoCs. The details of data collection are described in the Supporting Information: Data for SoC Mapping of the Cell section.

capability of extracting the SoC value from the complicated ultrasonic waveform.

Combining FNN algorithms with the progressive ultrasonic scanning technique, the SoC distribution map during charge/discharge can be obtained. The resolution of the SoC map is determined by the diameter of the focused ultrasound beam, which is around 1 mm. Since the tabs significantly disturb ultrasound transmission, the near tab areas were cut out of the SoC maps.

The obtained SoC distribution maps of Cell #4 during the charge process are shown in Figure 4a. The colors in these maps indicate the differences between the FNN estimated local SoC and general SoC, where blue indicates that the local SoC is smaller than the general SoC, and red indicates that the local SoC is higher than the general SoC. The color varies more significantly in the maps of middle SoC stages, indicating that the SoC distributions at these stages were broader.

Figure 4b exhibits the statistic distribution of local SoCs at different general SoCs. At each general SoC, the histogram of local SoCs roughly conforms to a Gaussian distribution. The local SoC distribution first broadened and then narrowed as the general SoC increased. The standard deviation (STD) of SoC in one cell reached a maximum of about 5.5% in the middle SoC region. Such a phenomenon is because the slope of the voltage-SoC curve is flatter in the middle SoC region, indicating that the cell voltage is not sensitive to SoC change, which leads to a larger SoC variation possibility at a certain voltage.

In summary, nondestructive *in situ* SoC mapping of the pouch-type LIB is realized via ultrasonic scanning and FNN-based deep learning analysis. The characteristics of the transmitted ultrasonic signal, e.g., ToF, intensity, and frequency, show some correlation with the SoC of the cell. However, it is hard to precisely estimate the SoC with a single ultrasonic characteristic because these correlations are not robust enough, especially for different cells. The FNN-based deep learning analysis of the entire waveform instead of fitting

with any single characteristic is an effective way to improve the SoC estimation reliability and extend its application to different cells. Verified by the ICP-OES test of the local lithium content, the RMSE of the FNN estimated SoC is narrowed down to 3.02%. Combining with the progressive scanning technique with a focused ultrasonic beam, SoC mapping with an in-plane resolution of 1 mm is achieved. The probability density histogram of the tested pouch cell is close to a Gaussian distribution. During the charge process, the SoC distribution first broadens and then narrows, indicating that the SoC distribution is more inhomogeneous in the voltage plateau region. This phenomenon agrees well with the common sense that the SoC inhomogeneity worsens when cell voltage is not sensitive to SoC change. Our method is a useful tool for LIB manufacturers to understand the battery failure mechanism[31] and hence to develop high-performance rechargeable batteries.[32−34]

■ ASSOCIATED CONTENT

ⓈI Supporting Information

The Supporting Information is available free of charge at https://pubs.acs.org/doi/10.1021/acsami.2c22210.

Detailed information on the testing procedure, data collection, neural network structure, and the hyperparameter optimization including variance filtering, weight initialization, dynamically adjusting the learning rate, and regularization items; additional data for acoustic response to SoC changing, data for FNN model training, data for FNN estimated local SoC, and data for SoC mapping of the cell; ICP-OES sample preparation and characterization; ICP-OES measured SoC calculation; iterative adjustment process data; Figure S1: diagram of the ultrasonic testing procedure; Figure S2: electrical experimental data; Figure S3: diagram of the acoustic data feature variance filtering; Figure S4: activation function and initial weight of the FNN; Figure S5: the raw single-point acoustic data and

the data after variance filtered; Figure S6: sample preparation and the measurements of the lithium content in the sample; Figure S7: comparison of the FNN estimated local SoC and ICP-OES measured local SoC value during the iterative adjustment process; Table S1: the ultrasonic battery scanning system component version and parameters: Table S2: cell structure details; Table S3: cycling protocol; Table S4: ICP-OES measured SoC calculation parameter value (PDF)

■ AUTHOR INFORMATION

Corresponding Authors

Yue Shen − *State Key Laboratory of Material Processing and Die & Mould Technology, School of Materials Science and Engineering, Huazhong University of Science and Technology, Wuhan, Hubei 430074, China*; Email: shenyue1213@hust.edu.cn

Yunhui Huang − *State Key Laboratory of Material Processing and Die & Mould Technology, School of Materials Science and Engineering, Huazhong University of Science and Technology, Wuhan, Hubei 430074, China*; ⓞ orcid.org/0000-0003-1687-1938; Email: huangyh@hust.edu.cn

Authors

Zhenyu Huang − *State Key Laboratory of Material Processing and Die & Mould Technology, School of Materials Science and Engineering, Huazhong University of Science and Technology, Wuhan, Hubei 430074, China; Wuxi Topsound Technology Co., Ltd., Wuxi, Jiangsu 214000, China;* ⓞ orcid.org/0000-0001-8286-3915

Yu Zhou − *Wuxi Topsound Technology Co., Ltd., Wuxi, Jiangsu 214000, China*

Zhe Deng − *Wuxi Topsound Technology Co., Ltd., Wuxi, Jiangsu 214000, China;* ⓞ orcid.org/0000-0002-3469-6208

Kai Huang − *State Key Laboratory of Material Processing and Die & Mould Technology, School of Materials Science and Engineering, Huazhong University of Science and Technology, Wuhan, Hubei 430074, China*

Mingkang Xu − *Wuxi Topsound Technology Co., Ltd., Wuxi, Jiangsu 214000, China*

Complete contact information is available at:
https://pubs.acs.org/10.1021/acsami.2c22210

Author Contributions

§Z.H. and Y.Z. contributed equally to this work. Z.H. built the ultrasonic battery scanning system, conceived and designed the experimental work, processed the acoustic data, and prepared the manuscript. Z.H. and Y.Z. built the FNN model. K.H. fabricated the pouch cells and ICP-OES tests. Z.D. and M.X. helped with the ultrasonic scanning. Y.S. and Y.H. supervised the overall project. All authors have given approval to the final version of the manuscript.

Notes

The authors declare no competing financial interest.

■ REFERENCES

(1) Robert, D.; Douillard, T.; Boulineau, A.; Brunetti, G.; Nowakowski, P.; Venet, D.; Bayle-Guillemaud, P.; Cayron, C. Multiscale phase mapping of LiFePO4-based electrodes by transmission electron microscopy and electron forward scattering diffraction. *ACS Nano* **2013**, *7*, 10887−10894.

(2) Holtz, M. E.; Yu, Y.; Gunceler, D.; Gao, J.; Sundararaman, R.; Schwarz, K. A.; Arias, T. A.; Abruña, H. D.; Muller, D. A. Nanoscale imaging of lithium ion distribution during in situ operation of battery electrode and electrolyte. *Nano Lett.* **2014**, *14*, 1453−1459.

(3) Fang, S.; Yan, M.; Hamers, R. J. Cell design and image analysis for in situ Raman mapping of inhomogeneous state-of-charge profiles in lithium-ion batteries. *J. Power Sources* **2017**, *352*, 18−25.

(4) Kostecki, R.; Lei, J.; McLarnon, F.; Shim, J.; Striebel, K. Diagnostic Evaluation of Detrimental Phenomena in High-Power Lithium-Ion Batteries. *J. Electrochem. Soc.* **2006**, *153*, A669.

(5) Nishi, T.; Nakai, H.; Kita, A. Visualization of the State-of-Charge Distribution in a LiCoO2 Cathode by In Situ Raman Imaging. *J. Electrochem. Soc.* **2013**, *160*, A1785.

(6) Nanda, J.; Remillard, J.; O'Neill, A.; Bernardi, D.; Ro, T.; Nietering, K. E.; Go, J.-Y.; Miller, T. J. Local State-of-Charge Mapping of Lithium-Ion Battery Electrodes. *Adv. Funct. Mater.* **2011**, *21*, 3282−3290.

(7) Lei, J.; McLarnon, F.; Kostecki, R. In Situ Raman Microscopy of Individual $LiNi_{0.8}Co_{0.15}Al_{0.05}O_2$ Particles in a Li-Ion Battery Composite Cathode. *J. Phys. Chem. B* **2005**, *109*, 952−957.

(8) Migge, S.; Sandmann, G.; Rahner, D.; Dietz, H.; Plieth, W. Studying lithium intercalation into graphite particles via in situ Raman spectroscopy and confocal microscopy. *J. Solid State Electrochem.* **2005**, *9*, 132−137.

(9) Mühlbauer, M. J.; Dolotko, O.; Hofmann, M.; Ehrenberg, H.; Senyshyn, A. Effect of fatigue/ageing on the lithium distribution in cylinder-type Li-ion batteries. *J. Power Sources* **2017**, *348*, 145−149.

(10) Cai, L.; An, K.; Feng, Z.; Liang, C.; Harris, S. J. In-situ observation of inhomogeneous degradation in large format Li-ion cells by neutron diffraction. *J. Power Sources* **2013**, *236*, 163−168.

(11) Petz, D.; Mühlbauer, M. J.; Baran, V.; Frost, M.; Schökel, A.; Paulmann, C.; Chen, Y.; Garcés, D.; Senyshyn, A. Lithium heterogeneities in cylinder-type Li-ion batteries − fatigue induced by cycling. *J. Power Sources* **2020**, *448*, 227466.

(12) Chueh, W. C.; El Gabaly, F.; Sugar, J. D.; Bartelt, N. C.; McDaniel, A. H.; Fenton, K. R.; Zavadil, K. R.; Tyliszczak, T.; Lai, W.; McCarty, K. F. Intercalation Pathway in Many-Particle $LiFePO_4$ Electrode Revealed by Nanoscale State-of-Charge Mapping. *Nano Lett.* **2013**, *13*, 866−872.

(13) Gent, W. E.; Li, Y.; Ahn, S.; Lim, J.; Liu, Y.; Wise, A. M.; Gopal, C. B.; Mueller, D. N.; Davis, R.; Weker, J. N.; Park, J.-H.; Doo, S.-K.; Chueh, W. C. Persistent State-of-Charge Heterogeneity in Relaxed, Partially Charged $Li_{1−x}Ni_{1/3}Co_{1/3}Mn_{1/3}O_2$ Secondary Particles. *Adv. Mater.* **2016**, *28*, 6631−6638.

(14) Mattei, G. S.; Li, Z.; Corrao, A. A.; Niu, C.; Zhang, Y.; Liaw, B.; Dickerson, C. C.; Xiao, J.; Dufek, E. J.; Khalifah, P. G. High-Energy Lateral Mapping (HELM) Studies of Inhomogeneity and Failure Mechanisms in NMC622/Li Pouch Cells. *Chem. Mater.* **2021**, *33*, 2378−2386.

(15) Cosby, M. R.; Carignan, G. M.; Li, Z.; Efaw, C. M.; Dickerson, C. C.; Yin, L.; Ren, Y.; Li, B.; Dufek, E. J.; Khalifah, P. G. Operando Synchrotron Studies of Inhomogeneity during Anode-Free Plating of Li Metal in Pouch Cell Batteries. *J. Electrochem. Soc.* **2022**, *169*, No. 020571.

(16) Wang, C.; Zhang, R.; Siu, C.; Ge, M.; Kisslinger, K.; Shin, Y.; Xin, H. L. Chemomechanically Stable Ultrahigh-Ni Single-Crystalline Cathodes with Improved Oxygen Retention and Delayed Phase Degradations. *Nano Lett.* **2021**, *21*, 9797−9804.

(17) Lee, E.; Lee, W.; Kim, J.; Kim, H.; Kim, M.; Yun, S.; Lee, S.; Kim, J.; Park, D.; Kim, D.; Yoon, W. S. The effect of high-temperature storage on the reaction heterogeneity of Ni-rich layered cathode materials. *Energy Storage Mater.* **2022**, *46*, 259−268.

(18) Maire, P.; Evans, A.; Kaiser, H.; Scheifele, W.; Novák, P. Colorimetric Determination of Lithium Content in Electrodes of Lithium-Ion Batteries. *J. Electrochem. Soc.* **2008**, *155*, A862−A865.

(19) Zhu, C.; Zhou, L.; Choi, M.; Baker, L. A. Mapping Surface Charge of Individual Microdomains with Scanning Ion Conductance Microscopy. *ChemElectroChem* **2018**, *5*, 2986−2990.

(20) Davies, G.; Knehr, K. W.; Van Tassell, B.; Hodson, T.; Biswas, S.; Hsieh, A. G.; Steingart, D. A. State of Charge and State of Health Estimation Using Electrochemical Acoustic Time of Flight Analysis. *J. Electrochem. Soc.* **2017**, *164*, A2746.

(21) Galiounas, E.; Tranter, T. G.; Owen, R. E.; Robinson, J. B.; Shearing, P. R.; Brett, D. J. Battery state-of-charge estimation using machine learning analysis of ultrasonic signatures. *Energy AI* **2022**, *10*, 100188.

(22) Hsieh, A. G.; Bhadra, S.; Hertzberg, B. J.; Gjeltema, P. J.; Goy, A.; Fleischer, J. W.; Steingart, D. A. Electrochemical-acoustic time of flight: in operando correlation of physical dynamics with battery charge and health. *Energy Environ. Sci.* **2015**, *8*, 1569−1577.

(23) Liu, Y.; Zhang, R.; Hao, W. Evaluation of the state of charge of lithium-ion batteries using ultrasonic guided waves and artificial neural network. *Ionics* **2022**, *28*, 3277−3288.

(24) Copley, R.; Cumming, D.; Wu, Y.; Dwyer-Joyce, R. Measurements and modelling of the response of an ultrasonic pulse to a lithium-ion battery as a precursor for state of charge estimation. *J. Energy Storage* **2021**, *36*, 102406.

(25) Gold, L.; Bach, T.; Virsik, W.; Schmitt, A.; Müller, J.; Staab, T. E. M.; Sextl, G. Probing lithium-ion batteries' state-of-charge using ultrasonic transmission − Concept and laboratory testing. *J. Power Sources* **2017**, *343*, 536−544.

(26) Popp, H.; Koller, M.; Keller, S.; Glanz, G.; Klambauer, R.; Bergmann, A. State Estimation Approach of Lithium-Ion Batteries by Simplified Ultrasonic Time-of-Flight Measurement. *IEEE Access* **2019**, *7*, 170992−171000.

(27) Ke, Q.; Jiang, S.; Li, W.; Lin, W.; Li, X.; Huang, H. Potential of ultrasonic time-of-flight and amplitude as the measurement for state of charge and physical changings of lithium-ion batteries. *J. Power Sources* **2022**, *549*, 232031.

(28) Meng, K.; Chen, X.; Zhang, W.; Chang, W.; Xu, J. A robust ultrasonic characterization methodology for lithium-ion batteries on frequency-domain damping analysis. *J. Power Sources* **2022**, *547*, 232003.

(29) Sun, H.; Muralidharan, N.; Amin, R.; Rathod, V.; Ramuhalli, P.; Belharouak, I. Ultrasonic nondestructive diagnosis of lithium-ion batteries with multiple frequencies. *J. Power Sources* **2022**, *549*, 232091.

(30) Hsu, C.-W.; Xiong, R.; Chen, N.-Y.; Li, J.; Tsou, N.-T. Deep neural network battery life and voltage prediction by using data of one cycle only. *Appl. Energy* **2022**, *306*, 118134.

(31) Hu, J.; Sun, Z.; Gao, Y.; Li, P.; Wu, Y.; Chen, S.; Wang, R.; Li, N.; Yang, W.; Shen, Y.; Bo, S.-H. 3D stress mapping reveals the origin of lithium-deposition heterogeneity in solid-state lithium-metal batteries. *Cell Rep. Phys. Sci.* **2022**, *3*, 100938.

(32) Li, Z.; Tian, F.; Li, Y.; Lei, D.; Wang, C. Zero-Strain Insertion Anode Material of Lithium-Ion Batteries. *Small* **2022**, 2204875.

(33) Feng, J.; Gao, Z.; Sheng, L.; Hao, Z.; Wang, F. R. Progress and perspective of interface design in garnet electrolyte-based all-solid-state batteries. *Carbon Energy* **2021**, *3*, 385−409.

(34) Yang, J.; Liu, G.; Avdeev, M.; Wan, H.; Han, F.; Shen, L.; Zou, Z.; Shi, S.; Hu, Y.-S.; Wang, C.; Yao, X. Ultrastable all-solid-state sodium rechargeable batteries. *ACS Energy Lett.* **2020**, *5*, 2835−2841.